Directional fine structure in absorption of white x rays: A tomographic interpretation

P. Korecki,[1,*] M. Tolkiehn,[2,3] D. V. Novikov,[2] G. Materlik,[4] and M. Szymonski[1]
[1]*M. Smoluchowski Institute of Physics, Jagiellonian University, Reymonta 4, 30-059 Kraków, Poland*
[2]*Hamburger Synchrotronstrahlungslabor HASYLAB at Deutsches Elektronen-Synchrotron DESY, Notkestraße 85, D-22603 Hamburg, Germany*
[3]*Advanced Photon Source, Argonne National Laboratory, Argonne, Illinois 60439, USA*
[4]*Diamond Light Source Limited, Chilton, Didcot Oxfordshire OX11 0DE, United Kingdom*
(Received 28 June 2006; revised manuscript received 11 September 2006; published 27 November 2006)

We discuss directional fine structure in absorption of white x rays for tomographic imaging of crystal structure at the atomic level. The interference between a direct x-ray beam and the secondary waves coherently scattered inside a specimen modifies the total wave field at the position of the absorbing atoms. For a white x-ray beam, the wave field variations cancel out by energy integration for all directions, except for the near forward scattering components, coinciding with the incident beam. Therefore, two-dimensional patterns of the angular-dependent fine structure in absorption of white x rays can be interpreted as real-space projections of atomic structure. In this work, we present a theory describing the directional fine structure in white x-ray absorption and a tomographic approach for crystal structure retrieval developed on its basis. The tomographic algorithm is applied to the experimental x-ray absorption data recorded for GaP crystals.

DOI: 10.1103/PhysRevB.74.184116 PACS number(s): 61.10.−i, 81.70.Tx, 42.30.Rx

I. INTRODUCTION

Analysis of the x-ray absorption fine structure is often used to obtain information about the geometrical structure of a sample at the atomic level. Usually, x-ray absorption fine structure is understood as the energy-dependent fine structure that arises from the interference of the excited outgoing photoelectron wave with the backscattered waves from neighboring atoms.[1] A straightforward analysis of the extended x-ray absorption fine structure (EXAFS) signal provides the information about the atomic bond distances. Apart from polarization effects, it does not depend on the relative direction between the x-ray beam and sample.

The angular-dependent, *directional* fine structure in x-ray absorption has a different origin and can also be used to obtain information about the structure of the absorbing sample. The interference between the direct x-ray beam and the waves coherently scattered inside the specimen modifies the x-ray wave field at the positions of the absorbing atoms. Thus, the absorption cross section is effectively modulated by the x-ray scattering. This effect can be used for a full three-dimensional analysis of spatial arrangements of atoms. In addition and contrary to most far-field diffraction methods,[2,3] the probing of the interference of the beams inside the sample can give access to the relative phase of the scattered waves in a way similar to holography. For a discussion of the fine structure in absorption arising from final- and initial-state effects, see Ref. 4.

Directional fine structure of x-ray absorption was initially implemented in the method of x-ray standing waves (XSW).[5,6] In XSW, absorption of particular atoms is measured by monitoring the secondary yield emitted incoherently from the sample as the crystal is rotated relative to the direction of the incident x-ray beam. This technique is predominantly used for perfect crystals. If the perfect crystal is brought into the Bragg condition, the dynamical interaction of primary and scattered waves[7] gives rise to a standing wave inside the crystal. The position of this standing wave, relative to the atomic planes, shifts with small detuning from the exact Bragg condition, which allows determination of the position of absorbing atoms within the unit cell inside the crystal and at surfaces.[8–10]

More recently, x-ray holographic methods[11–13] based on the internal detector principle[14–16] were demonstrated for direct three-dimensional imaging of local structure. In such methods, the directional fine structure of x-ray absorption is measured in a large solid angle and a holographic back transformation is used for a direct retrieval of structure around absorbing atoms.[17,18] XSW and holographic techniques have some common properties. Both methods use monochromatic x rays and sample the structural information in reciprocal space using similar experimental geometry. In addition, by virtue of the reciprocity theorem, they are connected to the Kossel diffraction lines.[19]

In recent work,[20,21] it was demonstrated that the patterns of the directional fine structure in x-ray absorption recorded using white x rays have a simple real-space interpretation. For a white x-ray beam, the wave field variations, due to interference of the incident beam with the waves scattered from single atoms, cancel out by energy integration for all directions, except for the forward scattering component, coinciding with the incident beam. Thus, the patterns of the directional fine structure in absorption of white x rays show distorted projections of atomic planes. In Ref. 21, a tomographic algorithm was proposed for a direct imaging of the crystal structure.

In this work, we present a theory that describes both the directional fine structure in absorption of polychromatic x rays and the principle of the tomographic approach for three-dimensional imaging of the crystal structure at the atomic level. The calculation is verified by comparison with the data recorded in experiment, preliminarily described in Ref. 21, performed for a GaP crystal.

The choice of sample was determined by several reasons. First of all, GaP crystallizes in the zinc blende structure and

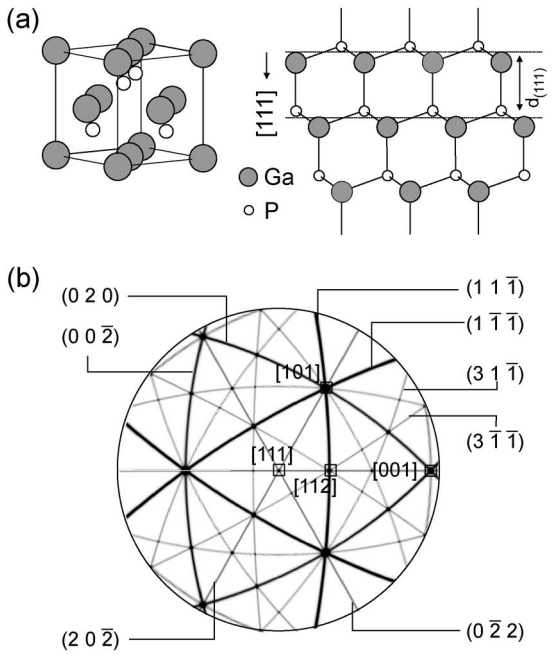

FIG. 1. (a) Structure of GaP. (b) Stereographic projection of the real space of GaP. Lines show intersections of crystallographic lattice planes with a sphere. Squares depict real-space directions.

has no inversion center of symmetry (see Fig. 1). Recently, the proposed methods of direct structure retrieval from holographic patterns[22,23] have had access only to the real parts of the structure factors and therefore cannot provide information about asymmetrical components of the structure, because of extinction and/or multiple scattering. Notably, one of the first experiments demonstrating the capabilities of XSW was performed for this crystal.[24] Secondly, high-quality GaP wafers are commercially available in both orientations along the [111] direction. This allows investigation of the extinction effects that can arise in holographic methods.[25] It will be shown that for white x-ray beams and short probing depths of secondary radiation, the pattern of directional fine structure is almost free of the extinction effects.

The paper is organized as follows. In Sec. II, a theory for the calculation of the directional fine structure in the absorption of white x rays is given. Furthermore, the principles of the tomographic algorithm for structure retrieval are presented. Section III contains a description of the experimental setup. Experimental data and analysis are presented in Sec. IV.

II. THEORY

A. Calculation of the directional fine structure in absorption of white x rays

Although the directional fine structure of absorption expressed in terms of reciprocal-lattice sums was presented in previous works for monochromatic x rays[22,26,27] with connection to x-ray holography, the white beam case was not discussed until now. In this subsection, formulas for calculation of the white beam case will be given.

In a general case, the absorption fine structure $\chi(\mathbf{k})$, resulting from interference of the x rays at the positions of absorbing atoms, can be defined by

$$\mu(\mathbf{k}) = \mu_0(k)[1 + \chi(\mathbf{k})], \tag{1}$$

where $\mu_0(k)$ denotes the absorption cross section calculated for an isolated atom. For the sake of simplicity, the calculation of $\chi(\mathbf{k})$ will be performed using scalar waves. For monochromatic illumination, the absorption fine structure of a single detecting atom placed at the origin can be written in the first Born approximation as[26]

$$\chi(\mathbf{k}) = -2r_0 \mathrm{Re} \int_{V_c} \rho(\mathbf{r}) \frac{e^{ikr}}{r} e^{i\mathbf{k}\cdot\mathbf{r}} dV, \tag{2}$$

where r_0 is the Thomson scattering length, $\rho(\mathbf{r})$ is the electron density of the sample, and the integral extends over the whole volume V_c of the sample. For periodic objects, the electron density of the sample can be written in terms of Fourier coefficients $F_\mathbf{H}$ as

$$\rho(\mathbf{r}) = \frac{1}{V} \sum_{\mathbf{H}} F_\mathbf{H} e^{i\mathbf{H}\cdot\mathbf{r}}, \quad F_\mathbf{H} = \int_V \rho(\mathbf{r}) e^{-i\mathbf{H}\cdot\mathbf{r}} dV, \tag{3}$$

where V is the volume of the unit cell.

Thus, after inserting Eq. (3) in Eq. (2), one obtains[22,26,27]

$$\chi(\mathbf{k}) = -\frac{8\pi r_0}{V} \mathrm{Re} \sum_{\mathbf{H}} F_\mathbf{H} [\chi^R_\mathbf{H}(\mathbf{k}) + i\chi^I_\mathbf{H}(\mathbf{k})], \tag{4}$$

where

$$\chi^R_\mathbf{H}(\mathbf{k}) = \frac{H^2 + 2\mathbf{H}\cdot\mathbf{k}}{(H^2 + 2\mathbf{H}\cdot\mathbf{k})^2 + (2k\Gamma)^2}, \tag{5}$$

$$\chi^I_\mathbf{H}(\mathbf{k}) = \frac{2k\Gamma}{(H^2 + 2\mathbf{H}\cdot\mathbf{k})^2 + (2k\Gamma)^2}. \tag{6}$$

Γ is a small positive number corresponding to the imaginary part of the wave vector having real part k.

The directional fine structure in absorption of polychromatic x rays can be calculated as[20,21]

$$\tilde{\chi}(\hat{\mathbf{k}}) = \int_0^\infty N(k)\chi(\mathbf{k})dk, \tag{7}$$

where $N(k)$ is the effective wave-vector spectrum sensed by the absorbing atom.

For the calculation of the analytical form of the directional fine structure for the polychromatic x-ray beam, we approximated the wave-vector spectrum $N(k)$ by a spectrum having a Lorentzian shape,

$$N_L(k) = \frac{1}{2\pi A} \frac{\Delta k}{(k - k_0)^2 + (\Delta k/2)^2}, \tag{8}$$

where $A = [\pi + 2\arctan(2k_0/\Delta k)]/(2\pi)$ ensures proper normalization in semi-infinite integrals.

From Eqs. (4) and (7), it follows that

$$\tilde{\chi}(\hat{\mathbf{k}}) = -\frac{8\pi r_0}{V}\,\mathrm{Re}\sum_{\mathbf{H}} F_{\mathbf{H}}[\tilde{\chi}^R_{\mathbf{H}}(\hat{\mathbf{k}}) + i\tilde{\chi}^I_{\mathbf{H}}(\hat{\mathbf{k}})], \tag{9}$$

where

$$\tilde{\chi}^{R,I}_{\mathbf{H}}(\hat{\mathbf{k}}) = \int_0^\infty N_L(k)\chi^{R,I}_{\mathbf{H}}(\mathbf{k})\mathbf{dk}. \tag{10}$$

For a wave-vector spectrum with $N_L(k)$ shape, the integrals in Eq. (10) can be calculated analytically.[28] The result contains only elementary functions but is lengthy and is not shown in explicit form. However, for $\Delta k \gg \Gamma$ a compact form of these expressions can by obtained by taking the limit $\Gamma \to 0$ *after* performing the integrations. Therefore, for the $N_L(k)$ spectrum,

$$\tilde{\chi}^R_{\mathbf{H}}(\hat{\mathbf{k}}) = \frac{H^2 + 2k_0\mathbf{H}\cdot\hat{\mathbf{k}}}{W} + \frac{\Delta k\mathbf{H}\cdot\hat{\mathbf{k}}}{2\pi AW}\ln[4\kappa_+^2(\mathbf{H}\cdot\hat{\mathbf{k}})^2/H^4] \tag{11}$$

and

$$\tilde{\chi}^I_{\mathbf{H}}(\hat{\mathbf{k}}) = \frac{\Delta k}{2AW}(|\mathbf{H}\cdot\hat{\mathbf{k}}| - \mathbf{H}\cdot\hat{\mathbf{k}}), \tag{12}$$

where

$$W = H^4 + 4k_0H^2\mathbf{H}\cdot\hat{\mathbf{k}} + 4\kappa_+^2(\mathbf{H}\cdot\hat{\mathbf{k}})^2 \tag{13}$$

and $\kappa_+ = \sqrt{k_0^2 + (\Delta k/2)^2}$. For an approximation of the wave-vector spectrum with multiple Lorentzians, a simple superposition can be used.

For negligible dispersion correction of x-ray scattering (i.e., for $F_{-\mathbf{H}} = F^*_{\mathbf{H}}$), Eq. (9) can be written as

$$\tilde{\chi}(\hat{\mathbf{k}}) = -\frac{4\pi r_0}{V}\sum_{\mathbf{H}} \tilde{\chi}_{\mathbf{H}}(\hat{\mathbf{k}}), \tag{14}$$

where

$$\tilde{\chi}_{\mathbf{H}}(\hat{\mathbf{k}}) = \mathrm{Re}(F_{\mathbf{H}})\tilde{\chi}^+_{\mathbf{H}}(\hat{\mathbf{k}}) - \mathrm{Im}(F_{\mathbf{H}})\tilde{\chi}^-_{\mathbf{H}}(\hat{\mathbf{k}}) \tag{15}$$

and

$$\tilde{\chi}^+_{\mathbf{H}}(\hat{\mathbf{k}}) = \tilde{\chi}^R_{\mathbf{H}}(\hat{\mathbf{k}}) + \tilde{\chi}^R_{-\mathbf{H}}(\hat{\mathbf{k}}). \tag{16}$$

$$\tilde{\chi}^-_{\mathbf{H}}(\hat{\mathbf{k}}) = \tilde{\chi}^I_{\mathbf{H}}(\hat{\mathbf{k}}) - \tilde{\chi}^I_{-\mathbf{H}}(\hat{\mathbf{k}}). \tag{17}$$

Figure 2 shows functions $\tilde{\chi}^{\pm}_{\mathbf{H}}$ calculated for different Lorentzian wave-vector spectra with $k_0 = 20$ Å^{-1} and various Δk values. The wave-vector spectra change from a narrow one ($\Delta k = 0.1$ Å^{-1}) through a "realistic" one ($\Delta k = 7.5$ Å^{-1}) to an almost perfect white spectrum ($\Delta k = 100$ Å^{-1}). The angle $\theta_{\mathbf{H}} = \arcsin(\hat{\mathbf{k}}\cdot\mathbf{H})$ is the deviation from the lattice plane direction and $d_{\mathbf{H}} = 2\pi/H$ is the diffraction place spacing. Note that, for a particular energy spectrum, $\tilde{\chi}^{\pm}_{\mathbf{H}}$ functions have the following scaling properties:

$$\frac{\tilde{\chi}^{\pm}_{\mathbf{H}}(\sin\theta/H)}{\tilde{\chi}^{\pm}_{\mathbf{G}}(\sin\theta/G)} = \frac{G^2}{H^2}. \tag{18}$$

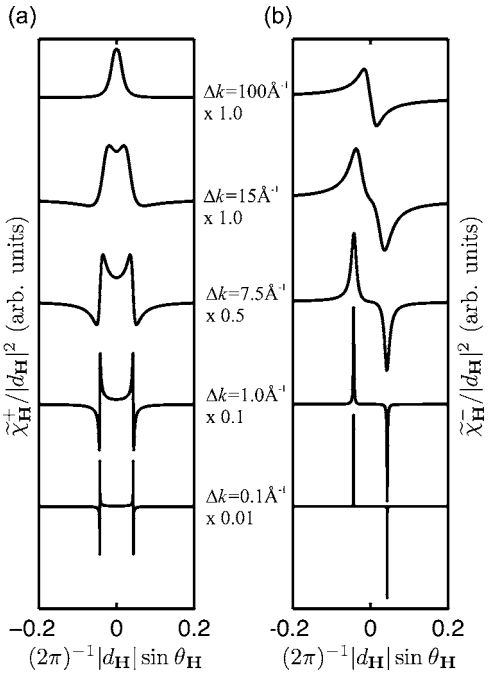

FIG. 2. Directional fine structure in x-ray absorption shown for various wave-vector spectra. Functions $\tilde{\chi}^+_{\mathbf{H}}$ (a) and $\tilde{\chi}^-_{\mathbf{H}}$ (b) are calculated for Lorentzian wave-vector spectra with $k_0 = 20$ Å^{-1} and for $\Delta k = (0.1, 1, 7.5, 15, 100)$ Å^{-1} (from bottom to top). The curves are magnified using factors of 0.01, 0.1, 0.5, 1, and 1.

For small Δk, the directional signal is located on two Bragg cones corresponding to **H** and **−H** vectors and has a shape similar to a pair of well separated kinematic Kossel or XSW lines.[19,23,26] As the energy spectrum becomes broader, the signal is also broadened, and the cones shift into the direction of the lattice plane. The position of the cones, which can be calculated from Eqs. (11) and (12), is

$$\Delta\theta_H = \arcsin\left(\frac{H}{2\kappa_+}\right). \tag{19}$$

Note that, for $\Delta k = 0$, this expression reduces to the Bragg condition $\lambda = 2d_H \sin\Delta\theta_H$, where λ is the x-ray wavelength. Therefore, Eq. (19) can be treated as a generalized Bragg-Kossel condition. For large Δk, the signals corresponding to **H** and **−H** vectors overlap and build a single intensity *band*, located on the great circle corresponding to the projection of a given lattice plane. These bands are similar to the bands observed in medium- and high-energy dynamical electron diffraction, which are known as Kikuchi bands.[2,29,30] For an almost perfect white spectrum, the remnant diffraction effects are totally flattened out. For a "realistic" case, they are still present but their magnitude is strongly reduced.

In fact, a band results from a superposition of $\tilde{\chi}^{\pm}_{\mathbf{H}}$ functions corresponding to the set of all colinear reciprocal-lattice vectors **H** with a given unit vector $\hat{n}$,

$$\tilde{\chi}_{\hat{\mathbf{n}}}(\theta_{\hat{\mathbf{n}}}) = -\frac{4\pi r_0}{V}\sum_{\mathbf{H}\|\hat{\mathbf{n}}} \tilde{\chi}_{\mathbf{H}}(\theta_{\hat{\mathbf{n}}}). \tag{20}$$

For sufficiently large samples [the simulations set the lower limit to clusters with radius $(10-20)a_0$, where a_0 is unit cell

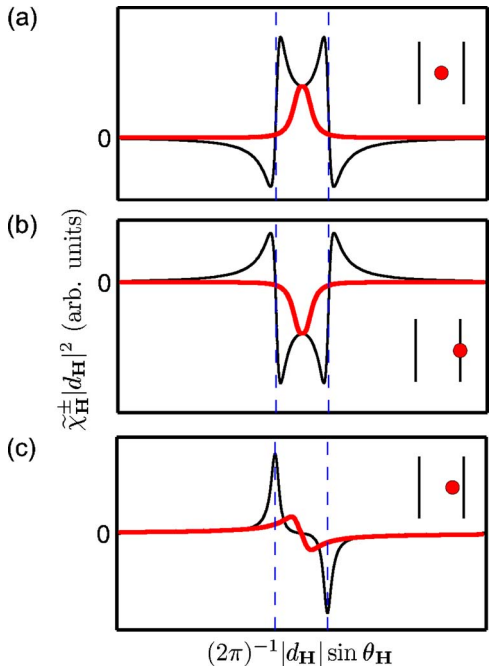

FIG. 3. (Color online). Directional fine structure in white x-ray absorption shown for various positions of the absorbing atoms relative to the lattice planes. (a,b) Symmetrical positions. (c) asymmetrical position. The curves are calculated for $k_0=20$ Å^{-1} and for $\Delta k=7.5$ Å^{-1} (thin black) and $\Delta k=100$ Å^{-1} (thick red). All curves are presented on the same scale. The positions of absorbing atoms relative to the lattice planes are shown in the insets. The vertical dashed lines show $\Delta\theta_{\hat{\mathbf{n}}}$ for $\Delta k=7.5$ Å^{-1}.

dimension], the strongest bands are well separated and a significant overlap between them occurs only at crossing points. The components of the band corresponding to a pair of $\pm\mathbf{H}$ vectors can be symmetric or asymmetric depending on the position of the absorbing atom relative to the planes forming the band, as is shown in Fig. 3.

At the center of the band *independently* on k_0 and Δk, one obtains

$$\tilde{\chi}_{\hat{\mathbf{n}}}(0) = -\frac{8\pi r_0}{V}\sum_{\mathbf{H}\|\hat{\mathbf{n}}}\frac{\mathrm{Re}\,F_{\mathbf{H}}}{H^2} = -\frac{\pi r_0 d^2}{3V}\{[\rho * g](0) - \bar{\rho}\}, \tag{21}$$

where * stands for the convolution integral

$$[\rho * g](z) = \int_{-d/2}^{d/2}\rho(x)g(z-x)dx, \tag{22}$$

and

$$\rho(z) = \int\int \rho(x,y,z)dx\,dy \tag{23}$$

is the projection of the electron density with $\hat{\mathbf{z}}\|\hat{\mathbf{n}}$ and $\hat{\mathbf{x}}\perp\hat{\mathbf{n}}$ and $\hat{\mathbf{x}}\perp\hat{\mathbf{y}}$, and

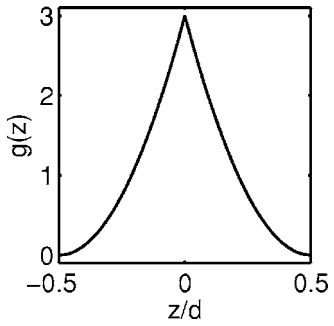

FIG. 4. Shape of the $g(z)$ function introduced in Eq. (25).

$$\bar{\rho} = \int \rho(z)dz \tag{24}$$

is the total electron number in the unit cell. Furthermore,

$$g(z) = \frac{12}{\pi^2}\,\mathrm{Re}[\mathrm{Li}_2(e^{i2\pi z/d})] + 1, \tag{25}$$

where Li_2 is a dilogarithmic integral and $d_{\hat{\mathbf{n}}}$ is the lattice plane spacing corresponding to the first-order reciprocal vector in the direction of $\hat{\mathbf{n}}$. For the derivation of this equation, see Sec. II C. Function $g(z)$ is shown in Fig. 4.

Equation (21) shows that at the center of the band, the signal is proportional to the projection of the electron density along the illumination direction. Therefore, the curves in Fig. 3 reflect coherent channeling and blocking/shadowing phenomena. The centers of isolated bands are completely free of the remnant diffraction effects. The convolution with $g(z)$ limits the resolution, even for a nearly perfect white x-ray beam. It is caused by the spherical character of scattered waves [cf. Eq. (2)]. Equation (21) does not depend of the parameters of the $N_L(k)$ spectrum. However, for a narrow wave-vector spectrum, the contribution at the center of the band coming from other bands can be much greater than the main signal and the real-space interpretation will therefore be hardly possible.

The formalism presented is valid for a single absorbing atom inside the unit cell. For several absorbing atoms this can be generalized, as shown in Refs. 23 and 25.

B. Probing the directional fine structure of white x-ray absorption via secondary yield

Absorption of a particular kind of atoms in the sample can be measured by monitoring the secondary yield (e.g., x-ray fluorescence, electron yield) incoherently emitted from these atoms as the sample is illuminated with x rays. The secondary yield $Y(\hat{\mathbf{k}})$ for a polychromatic incident x-ray beam can be calculated as

$$Y(\hat{\mathbf{k}}) = \int_0^\infty y(\mathbf{k})dk, \tag{26}$$

where

$$y(\mathbf{k}) = \int_0^d P(z,k)\frac{\mu(k)}{\cos\vartheta} I_0(z,\mathbf{k})dz \tag{27}$$

is the secondary yield produced by photons having wave vector $\mathbf{k}$. In Eq. (27), which is valid only in the kinematical approximation, $I_0(z,\mathbf{k})$ is the number of photons from the incident beam at a particular depth of the sample, which is assumed here to have a form of a plane parallel plate with thickness d. $P(z,k)$ describes, e.g., the emission of secondary electrons and in the simplest approximation is proportional to $\exp(-z/L)k$, where L is the electron escape depth.[31] ϑ is the angle between the beam direction and the normal to the sample surface. $\mu(k)$ is the absorption coefficient per unit volume of atoms contributing to the secondary yield and it contains the directional fine structure signal $\chi(\mathbf{k})$.

The secondary yield integrated over wave vectors can thus be written as

$$Y(\hat{\mathbf{k}}) = \frac{1}{\cos\vartheta}\int_0^\infty [1+\chi(\mathbf{k})]N(\mathbf{k})dk, \tag{28}$$

where

$$N(\mathbf{k}) = \mu_0(k)\int_0^d P(z,k)I_0(z,\mathbf{k})dz \tag{29}$$

is the effective wave-vector spectrum sensed by absorbing atoms [cf. Eq. (7)]. For the secondary yield characterized by a short escape depth (as compared to the absorption length of incident x rays), the incident beam $I_0(z,\mathbf{k})$ is hardly attenuated in the near-surface region. Therefore, one can assume that the shape of the effective wave-vector spectrum is almost independent of the direction of the incident beam, i.e., $N(\mathbf{k}) \approx N(k)$. Note that any significant deviation observed in experiment of $Y(\hat{\mathbf{k}})$ from $1/\cos\vartheta$ dependence would denote a failure of this approximation.

It must also be noted that for a general case, x-ray intensity inside the sample is determined by coherent[7,9] or incoherent[25,32] interaction of the primary and scattered beams inside the sample and can have complicated character resulting from multiple scattering, extinction, and total absorption effects. In addition, for monochromatic x-ray illumination even for small escape depth of the secondary yield, the directional fine structure of the secondary yield is strongly influenced by backscattered Bragg beams, which can dominate the fine structure of the observed patterns, as shown in Ref. 25. The integration of $\chi(\mathbf{k})$ over a broadband of wave vectors suppresses the integrated intensity of Bragg backscattering, which strongly depends on the energy, so that there is no significant backscattering observed at low escape depths. In Sec. III, it will be shown that the use of a white beam and of radiation with a short escape depth validates the use of the simple approximation used in this subsection and allows a tomographic approach for crystal structure determination.

C. Tomographic approach for imaging of crystal structure

In fact, Eq. (9) can already be used as a basis of a structure retrieval procedure using a linear regression algorithm[27] or a very similar algorithm presented in Ref. 22. However, for white x-ray illumination, the linear set of equations from Eq. (9) can become ill-posed: the $\chi_{\mathbf{H}}^{\pm}$ signals corresponding to the same band show strong overlap. On the other hand, the distorted real-space projections of atomic planes in the white x-ray beam patterns can be observed *directly*. Therefore, it is possible to establish a connection between the directional fine structure in white x-ray absorption and tomography.

In Sec. II A, it was shown that exactly at the center of the band, the directional x-ray absorption fine structure is simply related to the low-pass filtered projection of the electron density over a plane passing through the absorbing atom and coinciding with the illumination direction. In addition, there exists a relationship between the asymmetrical part of the structure with the asymmetrical components of the observed signal. Let us consider a single intensity band, determined by the unit vector $\hat{\mathbf{n}}$ being normal to the corresponding set of lattice planes and two quantities measured across the band from the experimental pattern $\chi(\hat{\mathbf{k}})$,

$$I_{\hat{\mathbf{n}}}^{\pm} = \int w^{\pm}(\theta_{\hat{\mathbf{n}}})\tilde{\chi}_{\hat{\mathbf{n}}}(\theta_{\hat{\mathbf{n}}})d\theta_{\hat{\mathbf{n}}}, \tag{30}$$

where $I_{\hat{\mathbf{n}}}^{+}$ measures the average intensity near the center of the band and $I_{\hat{\mathbf{n}}}^{-}$ its asymmetry. The angle $\theta_{\hat{\mathbf{n}}} = \arcsin(\hat{\mathbf{k}}\cdot\hat{\mathbf{n}})$ is the deviation from the center of the band and $w^{+}(\theta_{\hat{\mathbf{n}}})$ and $w^{-}(\theta_{\hat{\mathbf{n}}})$ are normalized even and odd rectangular window functions,

$$w^{+}(\theta) = \begin{cases} \dfrac{1}{2\Delta w^{+}} & \text{for } |\theta| \le \Delta w^{+} \\ 0 & \text{elsewhere,} \end{cases} \tag{31}$$

$$w^{-}(\theta) = \begin{cases} \dfrac{\operatorname{sgn}\theta}{2\Delta w^{-}} & \text{for } |\theta| \le \Delta w^{-} \\ 0 & \text{elsewhere.} \end{cases} \tag{32}$$

In order to enhance the signal and to reduce the overlapping of bands, the integrals of Eq. (30) should be averaged over the great circle. This can be done by numerical integration of the individual band or by using a linear regression algorithm to fit multiple $w^{\pm}$ functions to the data. The latter procedure will further reduce the band overlaps.

From Eqs. (14) and Eq. (30), it follows that

$$I_{\hat{\mathbf{n}}}^{+} = -\frac{4\pi r_0}{V}\sum_{\mathbf{H}\|\hat{\mathbf{n}}} \operatorname{Re}(F_{\mathbf{H}})G_{\mathbf{H}}^{+}, \tag{33}$$

$$I_{\hat{\mathbf{n}}}^{-} = \frac{4\pi r_0}{V}\sum_{\mathbf{H}\|\hat{\mathbf{n}}} \operatorname{Im}(F_{\mathbf{H}})G_{\mathbf{H}}^{-}, \tag{34}$$

where $\mathbf{H}=\mathbf{0}$ is excluded from the sum. The quantities

$$G_{\mathbf{H}}^{\pm} = \int_{-\pi/2}^{\pi/2} w^{\pm}(\theta_{\hat{\mathbf{n}}})\tilde{\chi}_{\mathbf{H}}^{\pm}(\theta_{\hat{\mathbf{n}}})d\theta_{\hat{\mathbf{n}}} \tag{35}$$

depend only on the length H of $\mathbf{H}$ and on the sign of $\mathbf{H}\cdot\hat{\mathbf{n}}$. They do not depend on the particular direction of $\mathbf{H}$. The choice of such simple shapes of $w^{\pm}$ functions is motivated by

the fact that for the $N_L(k)$ spectrum and for rectangular window functions, analytical expressions for both $G_{\mathbf{H}}^{+}$ and $G_{\mathbf{H}}^{-}$ can be obtained.

Further calculation is, for simplicity, performed for $\hat{\mathbf{n}} \| \hat{\mathbf{z}}$,

$$I_{\hat{\mathbf{z}}}^{+} = -\frac{4\pi r_0}{V} \sum_{h \neq 0} \mathrm{Re}(F_{00h}) G_h^{+}, \tag{36}$$

$$I_{\hat{\mathbf{z}}}^{-} = \frac{4\pi r_0}{V} \sum_{h \neq 0} \mathrm{Im}(F_{00h}) G_h^{-}. \tag{37}$$

Equations (36) and (37) can be analyzed using Plancherel's theorem. For periodic functions $f(z)=1/d\Sigma_h F_h \exp(ihz)$ and $g(z)=1/d\Sigma_h G_h \exp(ihz)$, where $h=n2\pi/d$ (with n being an integer), it holds that

$$\frac{1}{d} \sum_h F_h G_h^{*} = \int_{-d/2}^{d/2} f(z) g^{*}(z) dz. \tag{38}$$

Taking into account that

$$\rho(z) = \int \int \rho(x,y,z) dx\, dy = \frac{1}{d} \sum_h F_{00h} e^{ihz} \tag{39}$$

and the fact that G_h^{+} is a real even function of h and G_h^{-} is a real odd function of h, one obtains

$$I_{\hat{\mathbf{z}}}^{\pm} = -\frac{8\pi r_0}{V} \int_{-d/2}^{d/2} \rho(z) g^{\pm}(z) dz, \tag{40}$$

where

$$g^{+}(z) = \sum_{h>0} G_h^{+} \cos hz \tag{41}$$

and

$$g^{-}(z) = \sum_{h>0} G_h^{-} \sin hz. \tag{42}$$

In tomography, the object is reconstructed from its projections obtained for different illumination angles. In order to compare the results from Eq. (40) with the three-dimensional tomographic Radon transform, which is given by the plane integral[33,34]

$$\mathcal{R}_{\hat{\mathbf{n}}}[\rho](\zeta) = \int_V \rho(\mathbf{r}) \delta(\zeta - \hat{\mathbf{n}} \cdot \mathbf{r}) dV, \tag{43}$$

where $\hat{\mathbf{n}}$ is normal to the integration plane and ζ is the plane offset, one defines the following quantities:

$$I_{\hat{\mathbf{z}}}^{\pm}(\zeta) := \mp \frac{8\pi r_0}{V} \int_{-\infty}^{\infty} [\rho * g^{\pm}](z) \delta(\zeta - z) dz, \tag{44}$$

where δ is the Dirac delta distribution. Obviously $I_{\hat{\mathbf{z}}}^{\pm} = I_{\hat{\mathbf{z}}}^{\pm}(0)$. Also, due to the periodicity of $g^{\pm}$ and ρ, $I_{\hat{\mathbf{z}}}^{\pm}(m\,d) = I_{\hat{\mathbf{z}}}^{\pm}$ for all integer m. For arbitrary directions of $\hat{\mathbf{n}}$, definition (44) can be generalized to

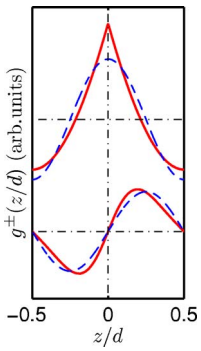

FIG. 5. (Color online). Shape of the $g^{+}(z)$ (top) and $g^{-}(z)$ functions (bottom) calculated for $k=20$ Å^{-1} and $\Delta k=7.5$ Å^{-1} and for $\Delta w^{+}=\Delta\theta_{\hat{\mathbf{n}}}/2$ and $\Delta w^{-}=2\Delta\theta_{\hat{\mathbf{n}}}$. For reference, $\cos(2\pi z/d)$ and $\sin(2\pi z/d)$ functions are shown as dashed lines. The dash-dotted lines show the zero levels.

$$I_{\hat{\mathbf{n}}}^{\pm}(\zeta) = \mp \frac{8\pi r_0}{V} \int_V [\rho * g_3^{\pm}](\mathbf{r}) \delta(\zeta - \hat{\mathbf{n}} \cdot \mathbf{r}) dV, \tag{45}$$

where

$$g_3^{\pm}(\mathbf{r}) = g^{\pm}(\hat{\mathbf{n}} \cdot \mathbf{r}) \delta(\mathbf{r}_{\perp}) \tag{46}$$

and $\mathbf{r}_{\perp}$ is the coordinate in the plane perpendicular to $\hat{\mathbf{n}}$. The integrals in Eq. (45) are Radon transforms of $\rho * g^{\pm}$. Finally, for ζ being a multiple of the lattice plane spacing $d_{\hat{\mathbf{n}}}$, one has

$$\mathcal{R}_{\hat{\mathbf{n}}}[\rho * g^{\pm}](m\, d_{\hat{\mathbf{n}}}) = \mp \frac{V}{8\pi r_0} I_{\hat{\mathbf{n}}}^{\pm} \tag{47}$$

for all integer m.

This result means that the quantities $I^{\pm}$ are related to the Radon transforms of the sample and that the knowledge of $g^{\pm}$ is crucial for the reconstruction of the sample structure. The shape of these function depends mainly on the widths $\Delta w^{\pm}$ of the window functions used in Eq. (30) and weakly (if $\Delta w^{\pm}$ are proportional to $\Delta\theta_{\hat{\mathbf{n}}}$) on the wave-vector spectrum of the incident beam. As seen from Fig. 3 and from Eq. (21), Δw^{+} should be chosen as small as possible. However, a small Δw^{+} denotes a small signal-to-background ratio and the optimal value of Δw^{+} was found to lie in the interval $(\Delta\theta_{\hat{\mathbf{n}}}/4, \Delta\theta_{\hat{\mathbf{n}}})$, where $\Delta\theta_{\hat{\mathbf{n}}}$ is the angle derived from Eq. (19), corresponding to the first-order reciprocal vector $\mathbf{H} \| \hat{\mathbf{n}}$. For larger values of Δw^{+} (i.e., for $\Delta w^{+} > \Delta\theta_{\hat{\mathbf{n}}}$), the positive and negative parts of the $\tilde{\chi}_{\mathbf{H}}^{+}$ functions can cancel and reduce the measurable signal. On the other hand, in order to efficiently measure the asymmetry of the bands, Δw^{-} should be chosen as large as possible. In a practical case, Δw^{-} is limited by the overlap with other bands and its optimal value was found to lie in the interval $(2\Delta\theta_{\mathbf{n}}, 4\Delta\theta_{\mathbf{n}})$. It should also be noted that the widths $\Delta w^{\pm}$ can be set based on experimental patterns, and the exact knowledge of the wave-vector spectrum, which defines $\Delta\theta_{\hat{\mathbf{n}}}$, is not required. Examples of $g^{\pm}$ functions calculated for the Lorentz wave-vector spectrum with $k_0=20$ Å^{-1} and $\Delta k=7.5$ Å^{-1} are shown in Fig. 5. Although the calculation was done for particular numerical values, the presented shapes of $g^{\pm}$ functions can be treated as quite universal. The changes of both the wave-vector spectrum and the widths of the window

functions within the described ranges do not influence the shape of these functions significantly.

As seen from Eq. (41) and from Fig. 5, for a properly chosen window function, the convolution $\rho * g^+$ can be interpreted as a low pass-filtered projection of the object or, more precisely, as its variation with respect to the average electron density in the unit cell. The second convolution $\rho * g^-$ can be rewritten as

$$[\rho * g^-](z) = -\frac{1}{\pi z} * [\rho * q^-](z) = -\mathcal{H}[\rho * q^-](z), \quad (48)$$

where $q^-(z) = \mathcal{H}g^-(z) = \Sigma_h G_h^- \cos hz$ and $\mathcal{H}$ stands for Hilbert transform. Since q^- is, similarly to g^+, an even function having monotonically decreasing Fourier coefficients, Eq. (48) describes the Hilbert transform of the low pass-filtered projection of the object.

The reconstruction of the object in tomography is based on the central slice theorem.[33,34] It states that the one-dimensional Fourier transform of a projection $p_{\hat{\mathbf{n}}}(d)$ with respect to d is equal to a radial line of the n-dimensional Fourier transform of the object, in the direction of $\hat{\mathbf{n}}$. If the projections are sampled for a full range of angles and offsets, one is able to fully reconstruct the object. However, in our case the projections are sampled for a discrete number of illumination angles $\hat{\mathbf{n}}$ and, more importantly, artificially "sampled" only for a discrete number of plane offsets. Therefore, only limited information about the structure can be obtained from Eq. (45).

First, the projections are "sampled" (hereafter the quotation marks will be omitted) only at $md_{\hat{\mathbf{n}}}$, where the odd components of the electron density vanish. Therefore, both I^+ and I^- from Eq. (45) are required for reconstruction. The first one (I^+) can be used to recover the even components of the electron density. As was shown in Eq. (48), the second Radon transform (I^-) samples the Hilbert transform of the electron density at the same plane offsets. Since the Hilbert transform interchanges the odd and even components of the signals without altering their amplitudes, one is able to recover the odd components as well. Second, in both equations the convolutions limit the spatial resolution. Since the widths of the $g^\pm$ functions are of the order of $d_{\hat{\mathbf{n}}}/2$, the spatial resolution will increase with an increasing number of bands used for analysis. Furthermore, the low-pass filtered projections $\rho * g^\pm$ are sampled with sampling intervals of $d_{\hat{\mathbf{n}}}$. These functions are not band-limited to frequency $2\pi/d_{\hat{\mathbf{n}}}$ and thus they are undersampled and some aliasing errors can occur.

Fourier transforms of $I^\pm$ are discrete and limited to a sphere with radius of $2\pi/d_{\hat{\mathbf{n}}}^{\min}$. Thus, direct application of the central slice theorem to Eq. (45) gives the even $\tilde{\rho}^+$ and odd $\tilde{\rho}^-$ low-pass filtered parts of the electron density,

$$\tilde{\rho}^+(\mathbf{r}) = \sum_{\hat{\mathbf{n}}} c_{\hat{\mathbf{n}}}^+ I_{\hat{\mathbf{n}}}^+ \cos\left[\frac{2\pi}{d_{\hat{\mathbf{n}}}}\hat{\mathbf{n}}\mathbf{r}\right], \quad (49)$$

$$\tilde{\rho}_-(\mathbf{r}) = \sum_{\hat{\mathbf{n}}} c_{\hat{\mathbf{n}}}^- I_{\hat{\mathbf{n}}}^- \sin\left[\frac{2\pi}{d_{\hat{\mathbf{n}}}}\hat{\mathbf{n}}\mathbf{r}\right], \quad (50)$$

where

$$c_{\hat{\mathbf{n}}}^\pm = -\frac{V}{8\pi r_0 G_{H_0}^\pm} \quad (51)$$

and $H_0 = 2\pi/d_{\hat{\mathbf{n}}}$ is the first-order reciprocal vector in the direction of $\hat{\mathbf{n}}$. The total image can be calculated as $\tilde{\rho}(\mathbf{r}) = \tilde{\rho}^+(\mathbf{r}) + \tilde{\rho}^-(\mathbf{r})$. The normalization constants $c_{\hat{\mathbf{n}}}^\pm$ are introduced to compensate for the decrease of the amplitude of the signal caused by the convolution with $g^\pm$ functions. They can be omitted, resulting in apodization of the reconstructed image.

The upper and much overestimated limit for aliasing errors in the reconstructed image can be calculated for point scatterers placed in a simple cubic lattice ($F_{\mathbf{H}} = 1$ for all $\mathbf{H}$) for $\Delta w^+ \to 0$ and for the g^+ function, which in the current idealized calculation is not band-limited. In such a case, the errors of reconstructing the low-pass filtered even component of the object electron density, normalized by the mean electron density $\bar{\rho}$, are $\Sigma_n 1/n^2 - 1 = \pi^2/6 - 1 \approx 0.64$. For the odd component, these errors are much smaller: the method of measuring the I^- integral makes the g^- function band-limited. The magnitudes of the aliasing errors (for point δ-like scatterers) can be seen as the deviation of the corresponding functions from sine and cosine as illustrated in Fig. 5. In realistic cases, the aliasing errors are greatly reduced. First, for $\Delta w^+ > 0$, the Fourier components $G_{\mathbf{H}}^+$ of the g^+ function decrease faster than $1/H^2$. Second, the electron distribution itself is a smooth function that makes the convolutions band-limited. Also, the thermal motions of atoms cause the further fall off of the high Fourier components of ρ. Thus the expected errors are of the order of several percent. Generally these errors will increase with increasing lattice plane spacing. For samples with large unit cells, these errors can be further decreased by repeating the tomographic algorithm using different widths of the window functions (e.g., $\Delta w^+ > \Delta\theta_{\mathbf{n}}$). This can significantly change the shape of the real-space function $g^\pm$ and will provide additional information. These can be understood by inspecting Eqs. (36) and (37). By changing $G_{\mathbf{H}}^\pm$ coefficients, one is able to solve the linear set of equations for $F_{\mathbf{H}}$.

Note that by using the tomographic algorithm, only the content of the unit cell can be determined. The information about the shape of the sample is lost already in Eq. (30).

III. DESCRIPTION OF EXPERIMENT

Two single-crystal GaP wafers (thickness 300 μm, both sides polished), cut from the same ingot, with orientations (111) (sample A) and $(\bar{1}\bar{1}\bar{1})$ (sample B), were used in the experiment. The polarity of the crystals was additionally checked after the experiment by chemical etching in $HCl(4):HNO_3(1)$ solution.

The directional fine structure in absorption of white x rays was measured using a white x-ray synchrotron beam (0.5×0.5 mm^2) produced by a bending magnet at beamline CEMO at the DORIS III storage ring in HASYLAB/DESY. A 10-mm-thick passive Al absorber was used to shape the broadband energy spectrum. The beam intensity was monitored with a photodiode operating in the current mode, which was placed directly in the beam. The average measured

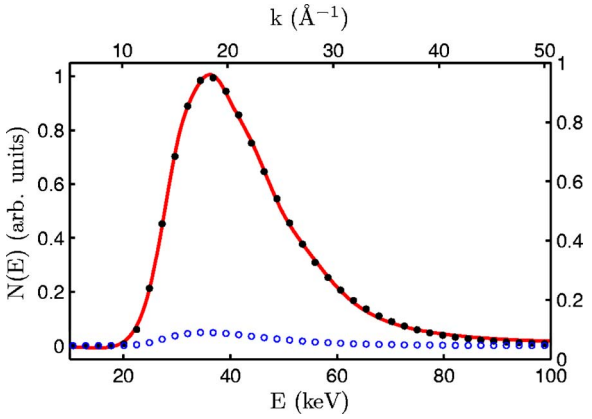

FIG. 6. (Color online). Calculated effective energy spectra probed by atoms emitting the secondary yield. The effective energy spectrum at Ga atoms calculated for parameters corresponding to experimental conditions is shown with solid circles. The solid line shows its approximation with five Lorenztian functions. The spectrum calculated for P atoms is shown with open circles.

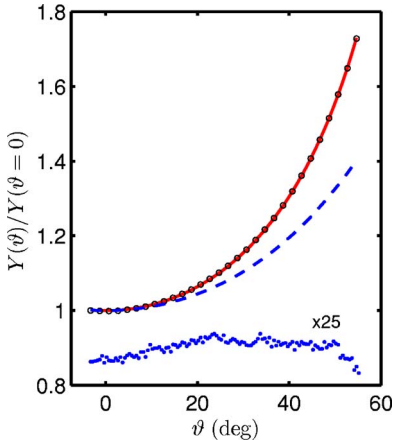

FIG. 7. (Color online). Directional dependence of the electron yield background. ϑ is the angle measured from normal to sample surface. Open circles show measured data. The solid line shows $1/\cos\vartheta$ dependence (no adjustable parameters were used for comparison). The dashed line shows the curve calculated for the secondary yield coming from the rear side of the sample. The magnified ($\times 25$) and shifted difference of experimental data and $1/\cos\vartheta$ is shown with points. The visible modulation of the difference signal is mainly due to directional fine structure.

monitor currents were on the order of 10 μA. Another photodiode was used for measurement of the auxiliary x-ray transmission signal, which was used for sample orientation and reference.

The sample, biased to −90 V, was placed inside a total electron yield detector flowed with He. The average measured sample currents were in the range of 10 nA, whereas the direction-dependent fine structure of the signal was at the level of 10 pA.

The ratio of absorption of the x rays on Ga and P atoms was estimated to be ~20 and the secondary yield was assumed to come predominately from Ga atoms providing the element sensitivity. The calculated effective energy spectrum at Ga and P atoms (see Sec. II B for details), which includes the synchrotron source emission characteristics, transmission of all elements placed in the beam, and the energy dependence of the absorption in the sample, is shown in Fig. 6. These data could be accurately fitted with a superposition of five Lorentzian functions, which allowed the modeling of the data accordingly to Sec. II A. For a simplified analysis, this spectrum could be replaced by a single Lorentzian with $k_0 \sim 20$ Å^{-1} and $\Delta k \sim 7.5$ Å^{-1}, which correspond to a "realistic" case in calculations of Sec. II A.

The electron detector signal was corrected for nonlinearity and normalized by the monitor signal. The nonlinearity was caused by the nonuniform electric field distribution in the vicinity of the sample surface.[35] Usually, electron yield detectors operating in the current mode use a flat collector electrode to acquire the emitted signal. In the present case, it turned out that such an electrode disturbed the small signal variations and had to be avoided. The nonlinearity factor was obtained from large discontinuities in the normalized signal occurring during injections of the x-ray beam. The correction for nonlinearity was absolutely necessary in order to efficiently remove the influence of the incident beam intensity fluctuations on the fine structure of the signal.

The detector was designed to allow for simultaneous measurement of the transmission signal. Because of that, a small contribution (less than several percent) to the electron yield was coming from the rear side of the sample. The calculation of the attenuation of the incident beam in the sample, which was verified by the measured ratio of the intensity detected by the monitor and transmission diode, gave the value of the incident-to-transmitted intensity ratio of ~0.4. However, the nonsymmetric design of the detector greatly increased the ratio of signals coming from the front and rear sides of the sample. This was experimentally checked by analysis of the angular dependence of the secondary yield and by analysis of a complimentary data set measured for a 5 μm epitaxial film of GaN/Al_2O_3. The recorded pattern showed, within the accuracy governed by noise, only the features characteristic of the GaN and not the rear side of the sapphire substrate.

For measuring the directional dependence of white x-ray absorption, the electron yield was collected while the sample, together with the detector, was rotated relative to the incident beam direction. The fast φ scan was performed continuously using an Eulerian cradle with an integration step of 0.3° around the sample normal. The inclination angle ϑ was changed step-by-step with 0.5° intervals. The maximum inclination angle was limited to 57° by the detector housing.

Four two-dimensional patterns were acquired for each wafer. The acquisition time of a single pattern was about 6 h. The slowly varying background was subtracted separately for each azimuthal scan using smoothing splines.[36] The patterns were symmetrized using rotation axes and mirror planes along the surface normal. The symmetrization procedure was performed in order to patch up some corrupted parts of the patterns, caused by inhomogeneities of the sample surface and of the detector entrance window.

IV. RESULTS AND DISCUSSION

Figure 7 shows the measured dependence of the electron

signal emitted from the GaP sample illuminated with a white x-ray beam as a function of angle ϑ between the beam direction and the normal to the surface of the sample. Although this slowly varying component of the signal has to be removed prior to analysis, it contains important information.

First, the very good coincidence of the measured signal with $1/\cos\vartheta$ confirms that the conditions of the experiment fulfill the assumptions presented in Sec. II B. Second, the negligible deviation proves that the parasitic signal coming from the rear side of the sample makes only a minor contribution to the total signal for all inclination angles.

The two-dimensional patterns of the directional fine structure in absorption of white x rays are presented in Fig. 8. The intensity scale, shown in colorbars, is normalized to the slowly varying background. All patterns are presented as stereographic projections. Because of ambiguous background removal, the parts of patterns near the pole were excluded from analysis.

The patterns recorded using the total electron yield for A and B samples are presented in Figs. 8(a) and 8(b), respectively. Figure 8(c) shows the difference of patterns presented in Figs. 8(a) and 8(b). The patterns recorded for A and B samples have slightly different signal-to-noise ratios and slightly different contrast. These are caused by the different qualities of the Ga and P rich surfaces of GaP resulting from the preparation procedure during manufacturing. Figure 8(d) shows a negative of the pattern recorded in the transmission geometry. This pattern was recorded on a reduced angular range.

The main features of the patterns recorded using the total electron yield are bands localized around the real-space projections of the crystal planes. The projections of the main crystal planes were displayed in Fig. 1 using the same stereographic projection. The maximal order of the band which can be clearly recognized in the experimental pattern is {113}. The variations of the band intensity agree with theoretical predictions described in Sec. II A and presented in Fig. 2. All the bands show deficiency in the intensity at the central positions. Thus, according to Figs. 3(a) and 3(b), one can directly see that the secondary yield is dominated by the electrons emitted from Ga atoms. The {111} bands display a significant asymmetry. This asymmetry is especially visible in the difference image obtained from patterns recorded for A and B sides. The specific character of the difference image shows that it cannot arise from the difference of contrast of both patterns, nor from possible misorientations of both patterns. The difference in the patterns recorded for A and B sides arises from the noncentrosymmetric structure of GaP

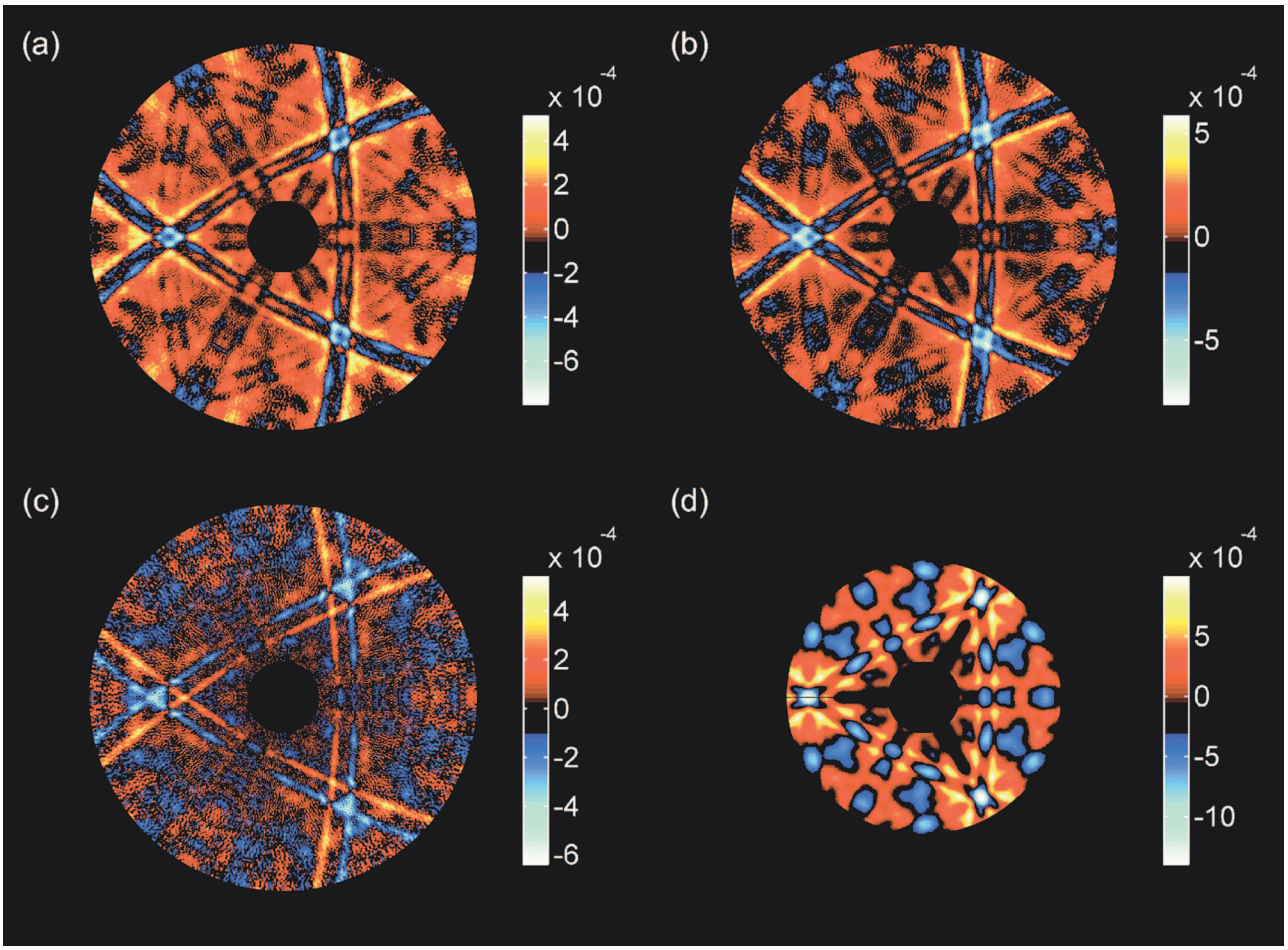

FIG. 8. (Color). Directional fine structure in absorption of white x-rays recorded for GaP. (a) Pattern recorded for (111) sample using total electron yield. (b) Pattern recorded for $(\bar{1}\bar{1}\bar{1})$ sample using total electron yield. (c) Difference of patterns recorded for (111) and $(\bar{1}\bar{1}\bar{1})$ samples. (d) Pattern recorded for (111) sample in transmission geometry.

and contains only the information about the P sublattice. The asymmetric shape of the bands is directly connected to different positions of the P planes with respect to the Ga planes [cf. Figs. 1(a) and Fig. 3(c)] and to resulting different real-space projections of P planes imaged relative to Ga atoms. Therefore, the asymmetry of the {111} band allows one to directly see the polarity of the sample. In XH and in Kikuchi electron diffraction, the asymmetry of the bands can also originate from dynamical extinction effects and does not ultimately arise from structural differences.[25,29] Here, a direct comparison of the data, recorded in the same condition for both crystal orientations, shows that the asymmetry comes solely from structural effects.

Figure 8(d) shows the directional pattern recorded in transmission geometry. Although the pattern has the same symmetry as patterns measured with total electron yield, it shows different fine structure and none of the observed bands display asymmetry. The data recorded in the transmission geometry can be dominated by pure x-ray scattering effects and cannot be treated as absorption patterns.[37–41]

The patterns shown in Figs. 8(a) and 8(b) were subsequently analyzed using the proposed tomographic algorithm. The intensity (I^+) and asymmetry (I^-) were measured for 21 different bands using the fit procedure described in the Appendix. Missing data were obtained via symmetry relations. The electron density distribution was restored according to Eqs. (49) and (50).

The electron density distribution that was restored from the experimental pattern is shown in Fig. 9. The reconstructed data show maxima at the positions of Ga and P atoms. The additional small maxima, especially visible in the cut shown in Fig. 9(b), are images of Ga atoms as seen from P atoms. They result from a nonzero contribution of the P atoms absorption to the total electron yield. They could be avoided by the detection of characteristic radiation. Meanwhile, the intensity of these artifacts can be used to estimate the sensitivity of the method for detecting low-Z elements at the level of at least three electrons per atom. The spatial resolution is limited by the lattice spacing of the analyzed bands having highest order i.e., to $d_{(113)}/2 \sim 0.8$ Å. The small deviations from the expected two-fold symmetry arise from experimental errors. The visible higher-frequency modulation of the real-space images does not correspond to true variation of electron density. It arises from truncation errors introduced in the tomographic algorithm and by the finite number of observed bands. For the case of GaP, the errors introduced by the imperfections of the tomographic approach, described at the end of Sec. II C, are smaller or comparable to the errors caused by the noise present in the measured patterns.

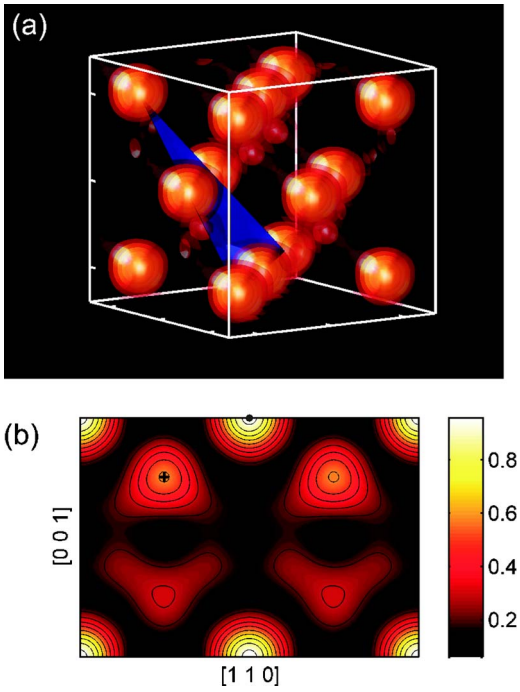

FIG. 9. (Color online). Structure of GaP directly restored from experimental data using the tomographic algorithm. (a) Three-dimensional view presented using isosurfaces. The edges of the box are parallel to ⟨001⟩ directions. The axis ticks are separated by half of the lattice constant. The triangle shows the (111) plane. (c) Electron density cut along the (110) plane. The contour lines, superimposed on the image, are spaced by ~0.1 of the maximal value. The circle and cross show the positions of Ga and P atoms, respectively.

V. CONCLUSIONS

It was shown that the directional fine structure in absorption of white x rays can provide *real-space* information about structure at the atomic level. A concise theory that describes the directional fine structure in the absorption of white x rays for periodic samples was presented. A tomographic-like algorithm was proposed for direct three-dimensional imaging of the unit cell. Although the algorithm was tested for the simple structure of a binary semiconductor, the capacity for imaging of samples with and without a center of inversion was demonstrated.

In general, the approach presented cannot compete with the well developed methods of x-ray diffraction. For complicated systems with large unit cells, an overlap of multiple bands would prevent high-resolution analysis. However, using for detection a characteristic radiation could allow studies of dilute systems not accessible to x-ray diffraction methods due to low signal-to-noise ratio. It would also be interesting to check if the combination of patterns recorded in the absorption and transmission geometry could be used to solve the crystallographic patterns without using characteristic radiation.

In the future, the proposed approach could be used for a model-free determination of the impurity positions in imperfect crystals in a way similar to channeling experiments with high-energy electrons. Such experiments use a dynamical scattering theory and require a starting model of the structure.[42,43]

In addition, the experimental patterns recorded in this work resemble low- and medium-energy photoelectron, Auger, or Kikuchi electron diffraction patterns. Such methods are extensively used for the analysis of the structure of surfaces, interfaces, and thin films. The directional fine structure in absorption of white x rays and the tomographic algorithm take advantage of kinematical scattering of x rays. Although

many of the works applying low- and medium-energy electron diffraction use kinematical modeling[30,44,45] and kinematical algorithms[18,46] for structure retrieval, such kinematical scattering conditions[47] are hardly possible in forward scattering patterns observed in electron diffraction. Thus, the method presented could be used for a more detailed analysis of such structures using a delicate probe. Of course the kinematic scattering is accompanied by weak contrast of the patterns recorded with x rays. The use of more powerful radiation sources will, however, increase the photon flux by several orders of magnitude. More flux would allow detection of characteristic radiation instead of total electron yield. Due to the slow angular dependence of the measured signal, the systems under investigations could be highly imperfect. In principle, the algorithm presented could be used in point source geometry of low-energy electron microscopy.

The main limitation of the approach presented is the weak signal and resulting detector limitations. Also the systems under investigation may not contain any materials with absorption edges occurring at the central part of the effective energy spectrum. In our experimental setup, this allows us to access elements with absorption edges below 20 keV. However, for more intense or harder x-ray sources, this limit can be increased.

ACKNOWLEDGMENTS

This work was supported by Volkswagen Foundation, Federal Republic of Germany. Access to synchrotron radiation was supported by the European Community–Research Infrastructure Action under the FP6 "Structuring the European Research Area" Programme (through the Integrated Infrastructure Initiative "Integrating Activity on Synchrotron and Free Electron Laser Science"), Contract No. RII3-CT-2004-506008. The authors would like to thank M. Targosz for the sample preparation, characterization, and AFM measurements and Yoshinori Nishino and Alec Sandy for helpful discussions. The engineers at the Institute of Physics (P. Piatkowski, and K. Pena) and at HASYLAB (H.-G. Schmidt) are acknowledged for help in designing the experimental setup and for support during beamtime.

APPENDIX

Since Eq. (30) measures the average value of the signal and its asymmetry near the center of the band, the numerical evaluation of integrals in Eq. (30) can be done by a simultaneous fit of the $w^{\pm}$ functions from Eqs. (31) and (32) to the measured data. This can by performed by solving the following matrix equation:[48]

$$\mathbf{Af} = \mathbf{b} \tag{A1}$$

with

$$\mathbf{A} = \mathbf{W}^T\mathbf{W}, \tag{A2}$$

$$\mathbf{b} = \mathbf{W}^T\mathbf{h}, \tag{A3}$$

where

$$\mathbf{W} = (\mathbf{W}^+ \ \mathbf{W}^-) \tag{A4}$$

and

$$\mathbf{f} = \begin{pmatrix} \mathbf{I}^+ \\ \mathbf{I}^- \end{pmatrix}. \tag{A5}$$

The elements of the column vector $\mathbf{h}$ are $h_j = \tilde{\chi}(\hat{\mathbf{k}}_j)$, i.e., the data measured at the jth point of the two-dimensional pattern. The elements of two-dimensional matrices $\mathbf{W}^+$ and $\mathbf{W}^-$ are $W^+_{ji} = w^+_i(\hat{\mathbf{k}}_j)$, $W^-_{ji} = w^-_i(\hat{\mathbf{k}}_j)$, i.e., the values of the window functions of the ith band $\hat{\mathbf{n}}_i$ evaluated at the jth point of the measured data. Finally, the elements of column vectors $\mathbf{I}^+$ and $\mathbf{I}^-$ are related to the desired values of the $I^{\pm}$ integrals. Therefore, the determination of the $I^{\pm}$ values is performed by calculating the inverse matrix $\mathbf{A}^{-1}$, which has dimension $(2N \times 2N)$, where N is the number of observed bands. The standard deviations of $I^{\pm}$ are connected to the diagonal elements of matrix $\mathbf{A}^{-1}$, whereas the covariances are the nondiagonal elements. It should be noted that direct integration of the experimental pattern in order to get the values of $I^{\pm}$ can lead to significant errors arising from band overlaps. The fit procedure is performed for all bands simultaneously so that such errors are minimized.

*Electronic address: korecki@if.uj.edu.pl

[1] P. A. Lee, P. H. Citrin, P. Eisenberger, and B. M. Kincaid, Rev. Mod. Phys. **53**, 769 (1981).
[2] J. Cowley, *Diffraction Physics* (North Holland, Amsterdam, 1975).
[3] Multiple wavelength anomalous and multibeam diffraction methods can provide phase information; see W. A. Hendrickson, Science **254**, 51 (1991); E. Weckert and K. Hummer, Acta Crystallogr. **53**, 108 (1997).
[4] Y. Nishino and G. Materlik, Phys. Rev. B **60**, 15074 (1999).
[5] J. A. Golovchenko, B. W. Batterman, and W. L. Brown, Phys. Rev. B **10**, 4239 (1974).
[6] M. J. Bedzyk and G. Materlik, Phys. Rev. B **32**, 6456 (1985).
[7] B. W. Batterman and H. Cole, Rev. Mod. Phys. **36**, 681 (1964).
[8] J. Zegenhagen, Surf. Sci. Rep. **18**, 199 (1993).
[9] I. A. Vartanyants and M. V. Kovalchuk, Rep. Prog. Phys. **64**, 1009 (2001).
[10] L. Cheng, P. Fenter, M. J. Bedzyk, and N. C. Sturchio, Phys. Rev. Lett. **90**, 255503 (2003).
[11] M. Tegze and G. Faigel, Nature (London) **380**, 49 (1996).
[12] G. Faigel and M. Tegze, Rep. Prog. Phys. **62**, 355 (1999).
[13] S. G. Bompadre, T. W. Petersen, and L. B. Sorensen, Phys. Rev. Lett. **83**, 2741 (1999).
[14] T. Gog, P. M. Len, G. Materlik, D. Bahr, C. S. Fadley, and C. Sanchez-Hanke, Phys. Rev. Lett. **76**, 3132 (1996).
[15] P. Korecki, J. Korecki, and T. Ślezak, Phys. Rev. Lett. **79**, 3518 (1997).
[16] K. Hayashi, M. Matsui, Y. Awakura, T. Kaneyoshi, H. Tanida, and

M. Ishii, Phys. Rev. B **63**, 041201(R) (2001).
[17] D. Gabor, Nature (London) **161**, 777 (1948).
[18] J. J. Barton, Phys. Rev. Lett. **61**, 1356 (1988).
[19] T. Gog, D. Bahr, and G. Materlik, Phys. Rev. B **51**, 6761 (1995).
[20] P. Korecki and G. Materlik, Phys. Rev. Lett. **86**, 2333 (2001).
[21] P. Korecki, M. Tolkiehn, D. V. Novikov, G. Materlik, and M. Szymonski, Phys. Rev. Lett. **96**, 035502 (2006).
[22] S. Marchesini *et al.*, Phys. Rev. B **66**, 094111 (2002).
[23] M. Tolkiehn, D. V. Novikov, and S. S. Fanchenko, Phys. Rev. B **71**, 165404 (2005).
[24] P. Trucano, Phys. Rev. B **13**, 2524 (1976).
[25] P. Korecki, D. V. Novikov, M. Tolkiehn, and G. Materlik, Phys. Rev. B **69**, 184103 (2004).
[26] B. Adams, D. V. Novikov, T. Hiort, G. Materlik, and E. Kossel, Phys. Rev. B **57**, 7526 (1998).
[27] F. N. Chukhovskii and A. M. Poliakov, Acta Crystallogr. **59**, 109 (2003).
[28] See EPAPS Document No. E-PRBMDO-74-010642 for the solution of these integrals. For more information on EPAPS, see http://www.aip.org/pubservs/epaps.html.
[29] B. Fultz and J. Howe, *Transmission Electron Microscopy and Diffractometry of Materials* (Springer, Berlin, 2002).
[30] J. Osterwalder, T. Greber, A. Stuck, and L. Schlapbach, Phys. Rev. B **44**, 13764 (1991).
[31] H. Henneken, F. Scholze, and G. Ulm, J. Appl. Phys. **87**, 257 (2000).
[32] V. F. Sears, Acta Crystallogr. **53**, 35 (1997).
[33] F. Natterer, *The Mathematics of Computerized Tomography* (Wiley, Chichester, 1986).
[34] A. C. Kak and M. Slaney, *Principles of Computerized Tomographic Imaging* (IEEE Press, Piscataway, NJ, 1988).
[35] W. T. Elam, J. P. Kirkland, R. A. Neiser, and P. D. Wolf, Phys. Rev. B **38**, 26 (1988).
[36] C. de Boor, *A Practical Guide to Splines*, Vol. 27 of Applied Math. Sciences (Springer Verlag, New York, 2001).
[37] Y. Nishino, T. Ishikawa, M. Suzuki, N. Kawamura, P. Kappen, P. Korecki, N. Haack, and G. Materlik, Phys. Rev. B **66**, 113103 (2002).
[38] M. Kopecky, A. Lausi, E. Busetto, J. Kub, and A. Savoia, Phys. Rev. Lett. **88**, 185503 (2002).
[39] M. Tegze, G. Faigel, and S. Marchesini, Phys. Rev. Lett. **89**, 279601 (2002).
[40] M. Kopecky, A. Lausi, E. Busetto, J. Kub, and A. Savoia, Phys. Rev. Lett. **89**, 279602 (2002).
[41] G. Faigel, M. Tegze, G. Bortel, and L. Koszegi, Europhys. Lett. **61**, 201 (2003).
[42] J. Spence and J. Tafto, J. Microsc. **130**, 147 (1983).
[43] U. Wahl, E. Rita, J. G. Correia, A. C. Marques, E. Alves, and J. C. Soares, Phys. Rev. Lett. **95**, 215503 (2005).
[44] C. S. Fadley, Surf. Sci. Rep. **19**, 231 (1993).
[45] S. Mroz and M. Nowicki, Surf. Sci. **297**, 66 (1993).
[46] M. Seelmann-Eggebert, Phys. Rev. B **55**, 15842 (1997).
[47] J. Wider, F. Baumberger, M. Sambi, R. Gotter, A. Verdini, F. Bruno, D. Cvetko, A. Morgante, T. Greber, and J. Osterwalder, Phys. Rev. Lett. **86**, 2337 (2001).
[48] W. H. Press, B. P. Flannery, S. A. Teukolsky, and W. Vetterling, *Numerical Recipes: The Art of Scientific Computing* (Cambirdge Univ. Press, Cambridge, 1986).